JOURNAL OF GEOPHYSICAL RESEARCH, VOL. 102, NO. A10, PAGES 22,183–22,197, OCTOBER 1, 1997

Charge exchange near Mars: The solar wind absorption and energetic neutral atom production

E. Kallio[1] and J. G. Luhmann

Space Sciences Laboratory, University of California, Berkeley

S. Barabash

Swedish Institute of Space Physics, Kiruna

Abstract. Charge exchange between solar wind protons and neutral atmospheric atoms is expected to affect the solar wind interaction with Mars, but its influences and significance have only been touched upon in previous work. Here several features associated with the charge exchange process between the solar wind protons and Martian neutral upper atmospheres are described. The analysis is based on an empirical proton model derived from Phobos 2 observations interacting with the Martian atomic (H) and molecular (H_2) hydrogen, and oxygen (O) upper atmospheres representing solar minimum and solar maximum conditions. The region where the largest fraction of solar wind protons is lost by the charge exchange process is found to be a thin layer above the surface of Mars on the dayside resulting from charge exchange with the thermal oxygen. In general, the magnetosheath and "magnetosphere" (where the observed plasma takes on a different character in the Phobos 2 data) produce two distinguishable regions where the loss rate of solar wind protons is highest. Increasing solar activity increases the loss rate in the magnetosheath but decreases it in the magnetosphere. No significant increase of the absorption of the solar wind was found near the "magnetopause" suggesting that the decrease of the solar wind protons observed by Phobos 2 are not due to the charge exchange process. In addition to a reduction in the solar wind density, the charge exchange reaction results in energetic neutral atom (ENA) production. This paper considers some of the detailed properties expected for the ENA population at Mars. The ENA differential fluxes were found to be typically 10^6-10^7 cm^{-2} s^{-1} keV^{-1} in the energy range 0.01 - 1 keV. During solar minimum, the ENA production rate and ENA integral fluxes were found to be highest in the magnetosheath. At solar maximum the ENA production rate is highest in the magnetosphere, and ENA integral fluxes in the dayside magnetosphere appear to become comparable to the fluxes in the magnetosheath if the proton temperature in the magnetosphere is low. It is found that 1-3% of the original solar wind proton flux converts into ENAs before the bow shock. The ENAs produced upstream are undeflected and so may precipitate into the Martian upper atmosphere, depositing an energy flux of up to 3×10^9 eV cm^{-2} s^{-1} derived from the solar wind. These results both suggest the possible benefits of observing ENA fluxes around Mars and suggest the necessary parameters for detector design.

1. Introduction

Although the Phobos 2 mission provided unique information about the plasma and magnetic fields around Mars, some basic questions about the solar wind interaction remained unanswered. In particular, we still do not know what process or processes result in forming an obstacle to the solar wind: interaction with the planetary atmosphere, a weak intrinsic magnetic field, or the planetary ionosphere?

The role played by the Martian neutral atmosphere is an especially interesting question because Phobos 2 plasma measurements suggested that the Martian atmosphere may be important in the interaction process. In particular, the density of ions of Martian origin, especially O^+ ions, was found to be comparable to the proton density in large regions of the Martian tail [*Lundin et al.*, 1990] and on the dayside below ≈ 1000 km altitude [*Lundin et al.*, 1991]. Moreover, the proton density and velocity is much lower in the Martian "magnetosphere" than in the magnetosheath [see, e.g., *Lundin et al.*, 1990, 1991]. These latter features in the proton data do not appear to be the signature of the crossing of a true magnetopause because the Martian magnetotail appears to be "induced" like the Venusian magnetotail [*Yeroshenko et al.*, 1990]. We do not know whether a weak intrinsic magnetic field may be important in the solar wind interaction in subtle ways, for example, by causing reconnection near the planet [see *Shinagawa and Cravens*, 1992]. Nevertheless, it is certain that charge exchange between solar wind protons and atmospheric atoms occurs around Mars.

Charge exchange is expected to be very effective at the weakly or nonmagnetized Mars and Venus because the solar wind protons reach altitudes where the density of the neutral upper atmosphere is high. Interest in the role of charge exchange

[1] Now at Finnish Meteorological Institute, Geophysical Research, Helsinki.

Paper number 97JA01662.
0148-0227/97/97JA-01662$09.00

between solar wind protons and the Martian neutral upper atmosphere has recently arisen because the charge exchange process is expected to cause, at least qualitatively, effects on the plasma parameters similar to those observed near the planet. In charge exchange, a solar wind proton takes an electron from an atmospheric atom, producing an energetic hydrogen atom and a new, initially cold, ion. The density of solar wind protons thus decreases while the density of the ions of Martian origin increases. The newly born cold ions "mass load" the solar wind taking energy and momentum from the solar wind flow. As a result, the process decreases the proton flux, decreases the plasma velocity, and can change the ion composition.

The charge exchange process differs from the two other processes that cause mass loading of the solar wind and changes in the ion composition, namely, photoionization and electron impact ionization [see, e.g., *Zhang et al.,* 1993a] in important ways. While all three processes can change the ion composition of the plasma and cause mass loading which affects the flow, only charge exchange takes energy and momentum from the solar wind plasma by turning the solar wind protons into energetic neutral atoms (ENAs). ENAs can thus give direct information about the efficiency of the charge exchange process because the number of ENAs is equal to the number of solar wind protons absorbed. Furthermore, the energy of the ENAs is the energy lost from the solar wind proton flow because momentum is conserved in the charge exchange process.

The role charge exchange plays at Mars is still poorly understood, in part due to the limited information on the Martian neutral upper atmosphere, especially the neutral oxygen corona which has not been observed [see, e.g., *Nagy et al.,* 1990]. Plasma parameters near Mars, where the neutral upper atmosphere density is highest, such as particle flux, velocity, and temperature of the solar wind protons, are likewise not well known. All of these are important because the strength of the charge exchange process depends on the proton flux, proton energy (through the cross section energy dependence), and density and composition of the neutrals. Our assessment of how effective the charge exchange process at Mars is thus depends on global proton flux and velocity models and the neutral upper atmosphere models.

In this work the role and effects of the charge exchange process near Mars are studied by using a recently developed empirical flow model of solar wind protons near Mars [*Kallio,* 1996]. The model is based on Automatic Space Plasma Experiment with a Rotating Analyzer (ASPERA) particle instrument three-dimensional observations near Mars on board the Phobos 2 spacecraft in early 1989. This model is derived from the statistics of the observations and is not based on any assumptions about the physical processes that change the flow of solar wind protons. Most global solar wind proton flow models around Mars are based on gas dynamics [*Russell et al.,* 1983; *Ip et al.,* 1994], sometimes combined with other models to describe the conditions inside the "obstacle" [*Lichtenegger et al.,* 1997]. In previous analyses of the solar wind charge exchange near Mars, nearly all of the solar wind protons were found to be transformed near the Martian "magnetopause" [*Ip et al.,* 1994]. Moreover, the absorption rate of solar wind protons was found to be maximum near the subsolar point [*Lichtenegger et al.,* 1997]. Our use of an empirical model is expected to give somewhat different results concerning the role of the charge exchange process at Mars than obtained from these previous studies.

Here we use the ASPERA model to determine what percent of the solar wind protons are lost near Mars due to the charge exchange process. The density of the neutral upper atmosphere and therefore the strength of the charge exchange process depends on solar activity. We investigate the role of solar activity here by using atomic (H) and molecular (H_2) hydrogen and oxygen (O) densities derived for the solar minimum and solar maximum conditions. Charge exchange is expected to produce energetic hydrogen atoms at locations removed from the site of the ENA production [*Barabash et al.,* 1995]. In this paper we put special emphasis on the characteristics of the ENA environment and its dependence on proton flow parameters such as temperature and velocity and on the solar extreme ultraviolet flux. Our results may be considered a first approximation to a global ENA simulation for Mars.

Below we first summarize the features of the assumed models that are important in modeling the charge exchange process. We then describe the simulation results and the inferred effects including the percentage of solar wind protons absorbed, the loss rate of solar wind protons in different regions, the ENA environment, and the solar activity effects on the general picture. Finally, we briefly consider the possible atmospheric effects caused by ENA absorption in the deeper atmosphere of Mars.

2. Model Description

2.1. Velocity and Neutral Atmosphere Models

The empirical model of the proton flow is based on the ASPERA three-dimensional proton velocity measurements near Mars in early 1989 (see *Kallio* [1996] for details). The model is axially symmetric and models separately the streamlines (Figure 1a) and the speed of the protons (Figure 1b). It should be noted that the model does not give any other parameters without extra assumptions about how the other parameters are related to the proton velocity. Figures 1c and 1d show an example of the proton density and the proton particle flux calculated from the continuity equation in the case when there are no proton sinks or sources.

The velocity model includes a bow shock and a boundary, here called the magnetopause, where the plasma speed decreases. The innermost obstacle boundary adopted for simplicity is a sphere of radius 1.05 Martian radii ($\approx$ 170 km) above the surface with the properties of a tangential discontinuity because no plasma or field penetrates it. The region between the bow shock and the magnetopause is referred to as the magnetosheath, and the region between the magnetopause and the obstacle boundary as the magnetosphere (although there is no assumption made regarding the presence of a planetary magnetic field in this model, it is not a priori ruled out).

From the charge exchange process point of view the model has the following important features. The proton flux decreases at the magnetopause even without any proton sinks (Figure 1d). The model is an open model in that the streamlines penetrate the magnetopause. Moreover, in the magnetosphere on the dayside, the altitude of the streamlines decreases with increasing solar zenith angles (SZA). The model is an improved version of our original flow model [*Kallio,* 1996]. The main difference between this new flow model and our original empirical flow model is that now the streamlines penetrate the magnetopause in the wake as well as on the dayside. The most notable consequence of this difference is that the new model produces global magnetic field lines where the magnetosheath field joins smoothly to the tail field [see *Kallio and Koskinen,* 1997].

Our charge exchange model includes the atomic and the molecular hydrogen exosphere (both adopted from *Krasnopolsky and Gladstone* [1996]) and the nonthermal oxygen corona with

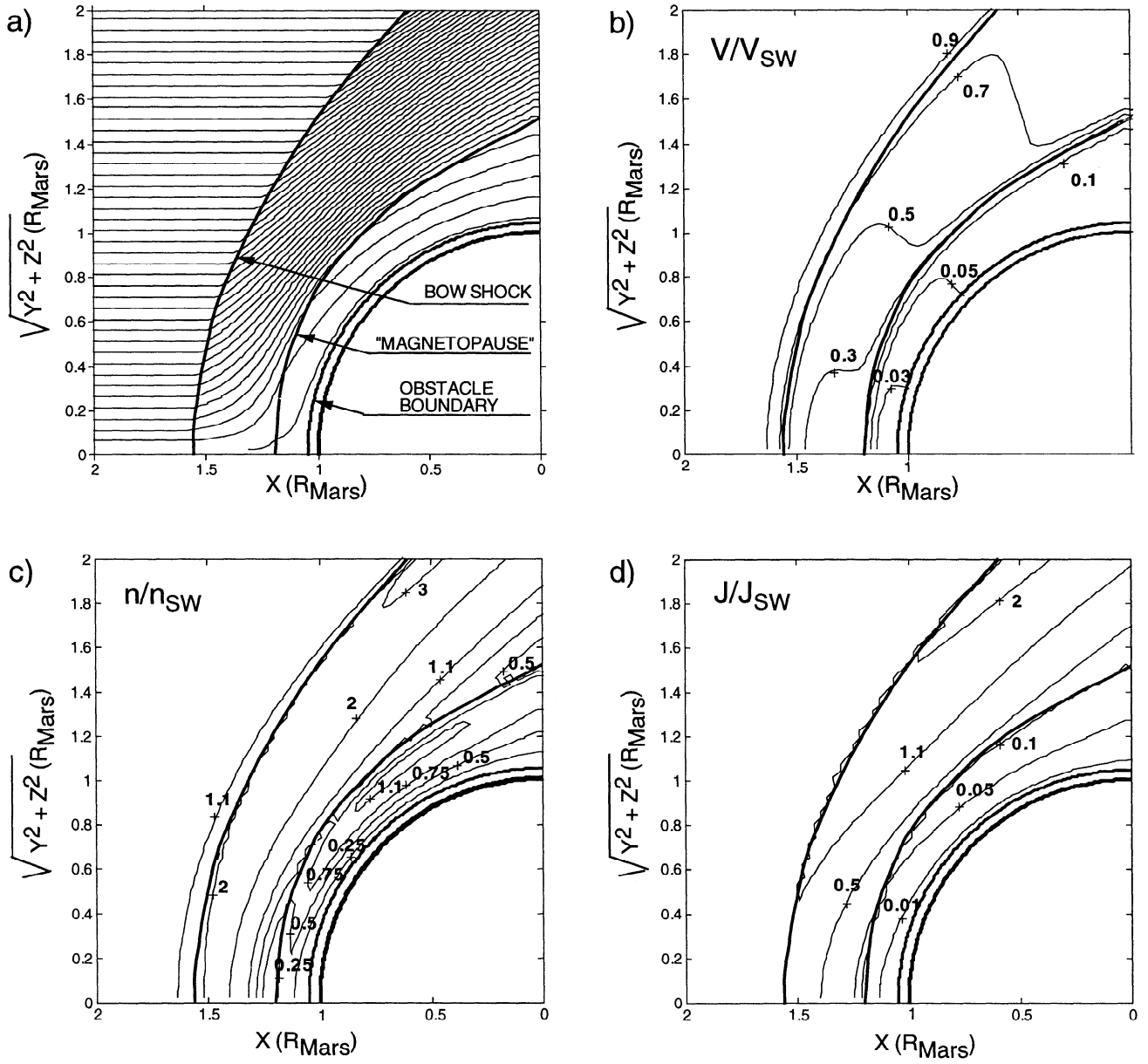

Figure 1. An empirical flow model of protons near Mars: (a) Streamlines, and (b) proton speed V/V_{SW}. (c) Density n/n_{SW} and (d) particle flux J/J_{SW} of the solar wind proton without proton sinks or sources. All values are normalized to undisturbed solar wind values.

the thermal component at lower altitudes (adopted from *Zhang et al.* [1993b]). Figure 2 shows the densities for low (Figure 2a) and high (Figure 2b) solar activity cases. In the latter case the extreme ultraviolet (EUV) flux is assumed to be 3 times higher that in the former case. Note that the density of hydrogen decreases with increasing EUV flux while the density of oxygen increases. This is a result of the very different origins of these species (thermal origin with Jeans escape for H, dissociative recombination of ionospheric O_2^+ for O).

In our simulation the atmospheric densities (n) are described by the following equation:

$$n = N \exp(\lambda - \lambda_o)\, \zeta(\lambda), \quad (1)$$

$$\lambda(r) \equiv GMm/kTr.$$

Here G is the gravitation constant, M is the mass of Mars, m is the atomic mass, k is the Boltzmann's constant, T is the exospheric temperature, r is the planetocentric distance, and $\lambda_o = \lambda(r_o)$. N is a constant value. The temperatures for H and H_2 were adopted from the atmosphere model [*Krasnopolsky and Gladstone,* 1996]: for solar minimum T was 200 K, and for solar maximum T was 350 K. Variable ζ is the partition function [see, e.g., *Chamberlain and Hunten,* 1987]. It should be noted that for planetocentric distances less than 5 R_{Mars} $\zeta(\lambda) \approx 1$ and thus $n \approx n_o \exp(\lambda - \lambda(r_O))$, where n_o is the density at $r = r_o$.

We used energy dependent cross sections (σ) to calculate the charge exchange processes between solar wind protons (H^+_{fast}) and the main atmospheric components H, H_2, and O:

$$\begin{aligned} H^+_{fast} + H &\rightarrow H_{fast} + H^+, \\ H^+_{fast} + O &\rightarrow H_{fast} + O^+, \\ H^+_{fast} + H_2 &\rightarrow H_{fast} + H_2^+. \end{aligned} \quad (2)$$

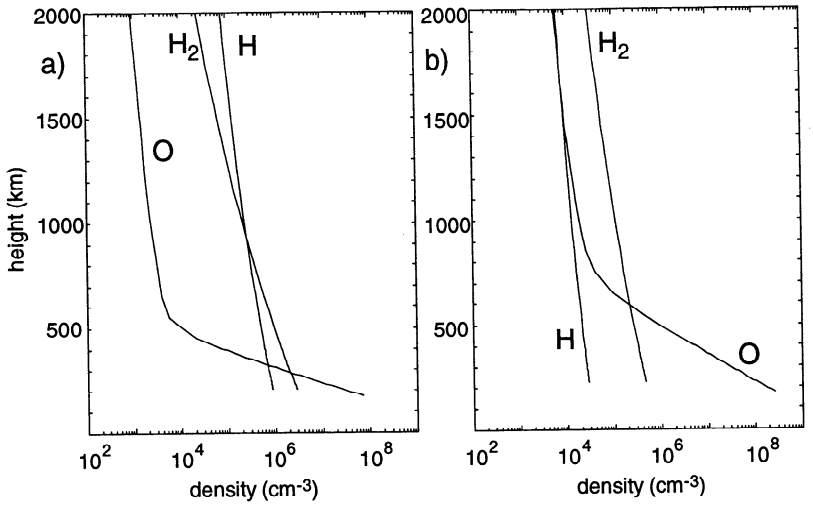

Figure 2. Models used for the Martian neutral atmosphere for (a) solar minimum (EUV1 model) and (b) solar maximum (EUV3 model). The solid curves show the density of atomic (H) and molecular hydrogen (H_2) and oxygen (O).

The charge exchange cross sections of protons on three main atmospheric components for the energy range 0.001 - 1 keV are shown in Figure 3. For completeness, the cross section for helium (He) is also shown because the density of helium exceeds the density of hydrogen at solar maximum near the surface [see *Krasnopolsky and Gladstone*, 1996]. However, due to a low cross section for the reaction H^+_{fast} + He we did not take into account that process.

In Figure 3 for the reactions between protons and H, H_2, and He the experimental results were fitted by the Chebyshev polynomials, and the parameters were taken from the compilation of *Barnett* [1990]. For the reaction between protons and O gas the experimental results from *Stebbings et al.* [1964] were used. The cross sections needed for this study extend to energies down to 0.12 eV for H, 2.6 eV for H_2, 99 eV for He and 30 eV for O, respectively. In order to cover the energy range down to 1 eV for all constituents we used a constant cross section for H_2 between 1 and 2.6 eV and continued the analytical extrapolation by *Stebbings et al.* [1964] down to 1 eV for O. This latter extrapolation seems to be reasonable, because it is a resonant interaction and thus should have a very smooth energy dependence.

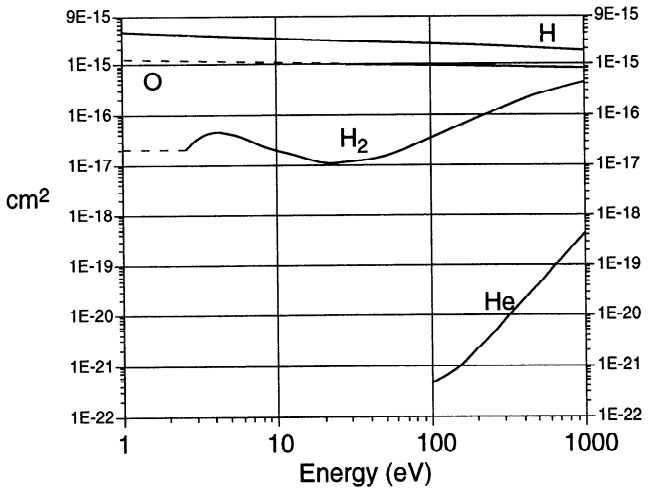

Figure 3. The charge exchange cross section of protons on the main gases in the Martian exosphere. The solid lines show analytical fits, and the dashed lines show the extrapolations. Helium was not used in our work due to its very small cross section. Read 9E-15 as 9×10^{-15}.

The total loss rate q_{tot} (cm^{-3} s^{-1}) of solar wind protons, or the production rate of neutral hydrogen of solar wind origin, depends on the particle flux of solar wind protons (j_{HSW}), the density of atomic hydrogen (n_H), molecular hydrogen (n_{H2}), and oxygen (n_O), and the charge exchange cross sections of the atomic hydrogen (σ_H), molecular hydrogen (σ_{H2}), and oxygen (σ_O):

$$q_{tot} = q_H + q_O + q_{H2} = j_{HSW} (\sigma_H n_H + \sigma_O n_O + \sigma_{H2} n_{H2}) \quad (3)$$

Here q_H, q_{H2}, and q_O, are the proton loss rates due to atomic hydrogen, molecular hydrogen, and oxygen charge exchange, respectively.

The solar wind proton flux, $j_{HSW}(r)$ can be obtained by integrating the particle continuity equation

$$\nabla \cdot (n_{HSW} U_H) = - n_{HSW} U_H \left(\sum_i \sigma_i n_i \right) \quad (4)$$

along streamlines. Here n_{HSW} is the density of the solar wind protons, U_H is the proton flow velocity, and the sum is over all atmospheric components which take part in the charge exchange process with solar wind protons. The result can be written in a form

$$n(r)_{HSW} = n_{SW} e^{-\int_\infty^r \frac{\nabla \cdot U_H}{U_H} ds} e^{-\sum_i \int_\infty^r n_i \sigma_i ds}$$

$$= N(r)_{HSW} e^{-\sum_i \int_\infty^r n_i \sigma_i ds} \quad (5)$$

Here n_{SW} is the density of protons in the solar wind, N_{HSW} is the density of solar wind protons if charge exchange did not occur (N_{HSW} is shown in Figure 1c), ds is the length along a streamline and the integration starts at the solar wind. Multiplying (5) by the proton velocity gives the proton particle flux:

$$j_{HSW}(\mathbf{r}) = n_{HSW}(\mathbf{r})\, U_H(\mathbf{r})$$
$$= N_{HSW}(\mathbf{r}) U_H(\mathbf{r})\, e^{-\sum_i \int_\infty^r n_i\, \sigma_i\, ds}$$
$$= J_{HSW}(\mathbf{r})\, e^{-\int_\infty^r \left(n_H(r')\,\sigma_H(E) + n_O(r')\,\sigma_O(E) + n_{H_2}(r')\,\sigma_{H_2}(E) \right) ds}$$
$$\equiv J_{HSW}(\mathbf{r})\, \xi_H(\mathbf{r}) \xi_O(\mathbf{r}) \xi_{H_2}(\mathbf{r}) \qquad (6)$$

Here j_{HSW} is the solar wind flux when the losses due to the charge exchange processes are taken into account and J_{HSW} (= $N_{HSW}U_H$) is the proton flux in the absence of charge exchange processes (J_{HSW} shown in Figure 1d). The exponential terms (ξ_H, ξ_O, ξ_{H2}) defined by (6) are associated with losses due to the charge exchange processes. The ξ values are between 1 and 0 where the unit corresponds to the solar wind fluxes if the charge exchange process does not occur. Zero indicates that all of the solar wind protons are absorbed. In (6), both the neutral density and the energy E depend on the position along the streamline. The energy which is needed to obtain the cross section at a given point $\mathbf{r}$ in the velocity model was calculated by assuming that the proton distribution function is Maxwellian (see below) and that the energy at the point $\mathbf{r}$, $E(\mathbf{r})$, is equal to $(m_p/2)U_H(\mathbf{r})^2 + (3/2)kT(\mathbf{r})$ (m_p is the proton mass, U_H is the proton bulk velocity, k is the Boltzmann's constant, and T is the proton temperature). The ξ values depend therefore on the proton bulk velocity and temperature. Note that for constant cross sections the ξ values would have depended on the streamline geometry alone.

2.2. Generation of ENAs

In our model the ENAs are produced from the solar wind protons only. Therefore in (3) we used the flux of the solar wind protons (j_{HSW}) and not the total proton flux. The total proton flux includes picked up H^+ ions produced by photoionization of the hydrogen exosphere and by the charge exchange process. Moreover, some of the ENAs, particularly near the planet, can turn back into fast protons when they collide with the Martian neutrals (see Appendix). This proton source produces energetic protons which can later produce new ENAs, which can then later produce new protons, etc. Modeling of the flow of the aforementioned locally born protons is, however, beyond the scope of this study.

In our model the starting points of ENAs are generated from the loss rates of solar wind protons by using the Monte Carlo method. The space around Mars is divided into a grid with a volume element dV whose size depends on the distance form the X axis. The probability p that an ENA is born in a given grid cell depends on the loss rate (q_{tot}) in this cell and on the volume dV of the cell. The flow model is axially symmetric; therefore the probability depends only on the axial distance x and the radius $R = \sqrt{y^2 + z^2}$. The probability p for an ENA to be born in the volume $dV = 2\,\pi R\, dx\, dR$ is therefore

$$p = p(x, R) = \frac{q_{tot} dV}{\int q_{tot} dV} = \frac{q_{tot}\, R\, dx dR}{\int q_{tot}\, R\, dx dR} \qquad (7)$$

Here the numerator gives the amount of ENAs produced in a volume dV per unit time. In our simulation dx and dR were 100 km. In the denominator the integration is performed over the full volume of our simulation box of $-2 < x < 2\ R_{Mars}$ and $R < 3\ R_{Mars}$ and gives the total number of ENAs generated per a unit time within our simulation box. We then launched 30,000 ENAs in the entire simulation box and used the obtained probability function p to get the number of starting points for each of 13,872 (=136 x 102) grid cells. The position of starting points within the grid cell was finally chosen randomly.

We then determined the velocity of the ENAs. We assumed that the starting velocity of the ENA is the same as the velocity of the solar wind proton that became the ENA because the momentum is conserved in the charge exchange reaction. We also assumed that the solar wind proton distribution function is Maxwellian everywhere. The velocity vector for the ENA is then obtained from the proton distribution function by choosing the velocity vector randomly within the three-dimensional Maxwellian distribution.

The proton bulk velocity (U_H) was taken from the empirical velocity model (Figure 1b), and we used a gas dynamic (GD) relationship to approximate the proton temperature (T_H) in the magnetosheath and in the magnetosphere. In a gas dynamic model the temperature (T_{GD}) can be obtained directly from the plasma speed [*Spreiter et al.*, 1966]:

$$T_{GD}(\mathbf{r}) = T_{SW}\left[1 + \frac{\gamma - 1}{2} M_{SW}^2 \left\{ 1 - \left(\frac{U_H(\mathbf{r})}{U_{SW}} \right)^2 \right\} \right] \qquad (8)$$

Here T_{GD} is the temperature of the plasma according to the GD model, U is the flow velocity at a given point $\mathbf{r}$, γ is the specific heat, and M_{SW}, T_{SW}, and U_{SW} are the sonic Mach number, the plasma temperature, and the velocity in the undisturbed solar wind, respectively. In our analysis we used 5/3 for γ.

Equation (8) has been found to give a rather realistic temperature jump for the solar wind protons at both the Martian [*Vaisberg et al.*, 1990] and Venusian [*Mihalov et al.*, 1980] bow shocks. However, at Venus, T_{GD} was found to be about twice as high as the observed ion temperatures, and at Mars T_{GD} was also higher than observed. In our model we thus used magnetosheath temperatures which were 0.5 times the gas dynamic value T_{GD}.

Not much is known about the temperature of the ions near the planet in the region called the magnetosphere in our model. There is no detailed analysis available about the proton temperature near the periapsis of Phobos 2 (≈860 km). However, according to the data from the Soviet Mars missions which had a periapsis near 1100 km, the ion velocity decreases at the same time as the ion temperature decreases to ≈10-20 eV near the planet in a region which was called the ion cushion (see review by *Vaisberg et al.* [1990]). This behavior cannot be explained by (8) because T_{GD} increases with decreasing U_H for a constant γ. Moreover, T_{GD} for a nearly stagnant plasma in which the flow energy is almost totally converted to thermal energy is tens of times higher than the solar wind temperature (see below), that is, much higher than observed.

The plasma temperature in the magnetosphere is best regarded as a free parameter of the simulation due to the aforementioned reasons. We thus calculated ENA starting velocities for two cases. In the hot temperature model (T_{MPhot}) the temperature in the magnetosphere and in the magnetosheath was assumed to be half of the gas dynamic temperature (Table 1). In the cold temperature model (T_{MPcold}) the temperature in the magnetosphere was decreased by a factor $(1/2)V_{MP}(\mathbf{r})^3$. Here V_{MP} is a hyperbolic tangent function which is 1 in the magnetosheath and decreases at the magnetopause smoothly to a value 0.1 at the obstacle boundary (see *Kallio* [1996, equations (6b) and (6c)] for definition for V_{MP}). This means that in the cold temperature model the temperature in the magnetosphere near the planet is

Table 1. The Adopted EUV and Temperature Models

	EUV Model	
	EUV1	EUV3
F10.7 cm flux	$64\ 10^{-22}$	$3 \times 64\ 10^{-22}$
[*Zhang et al.*, 1993b]	W m^{-2} Hz^{-1}	W m^{-2} Hz^{-1}
	T_H ($T_H = C_T T_{GD}$)	
	T_{MPhot}	T_{MPcold}
Magnetosheath	$C_T = 1/2$	$C_T = 1/2$
	=> $T_H \leq 170$ eV	=> $T_H \leq 170$ eV
Magnetosphere	$C_T = 1/2$	$C_T = (1/2)\ V_{MP}^3$
	=> $T_H \leq 170$ eV	=> $T_H << 170$ eV

The two EUV flux models determine which atmosphere models (solar minimum (EUV1) and maximum (EUV3)) were used. Temperature values show how the model proton temperatures (T_H) are related with the gas dynamic temperatures (T_{GD}) in (8) and what is the value of T_H in electron volts for the upstream parameters used in this work.

about 1/2000 of the gas dynamic temperature. Note also that because in the magnetosphere (U/U_{SW}) <≈ 0.1 (see Figure 1b), then $T_{GD} \approx 26.5 \times T_{sw} \approx 350$ eV for the solar wind parameters used in our simulation: T_{SW} =13 eV, and M_{SW} =8.8 (U_{SW}=400 km s^{-1}). This means that the proton temperatures in the magnetosphere can reach about 170 eV in the hot temperature model, and in the cold temperature model the temperatures can be less than 0.2 eV. Table 1 summarizes the adopted models.

2.3. Derivation of ENA Fluxes

In our simulation the ENAs are treated as test particles with straight-line trajectories. This is a good approximation because the energy in question is higher than the hydrogen escape energy (0.2 eV). The size of the space where ENAs were launched was $-2 < x < 2\ R_{Mars}$, and $0 < \sqrt{y^2+z^2} < 3\ R_{Mars}$. The ENA flux through the plane $x = 2\ R_{Mars}$ into the simulation box was calculated analytically by integration along the streamlines. The total ENA flux in a given cell is the sum of the ENA flux which was calculated analytically in a region $x > 2\ R_{Mars}$ and the ENA flux given by the Monte Carlo simulation within our simulation box. We assumed that ENAs are totally absorbed if they hit the obstacle surface of 170 km above the Martian surface. In reality, the loss of ENAs via electron stripping becomes important at slightly higher altitudes (see Appendix). However, in our simulation, ENAs are collected on a cylindrical area $|dA| = 2\pi\rho\ d\rho$ (see below) where $d\rho = 0.1\ R_{Mars} \approx 330$ km ($\rho = \sqrt{y^2+z^2}$) which is too large to observe this effect, and we disregard attenuation.

Figure 4 illustrates how the macroscopic parameters were calculated in our test particle simulation. It shows a trajectory of an ENA which penetrates a circular cylinder. The cylinder extends along the X axis dx and has a cross section $|dA| = 2\pi\rho\ d\rho$. The total number of trajectories in our simulation was 30,000. In Figure 4 the trajectory goes into the cylinder at the point P_{in} and it comes out at the point P_{out}. The circles show the positions of ENAs on the trajectory. All of these ENAs have the same velocity $\mathbf{V}_i$ and starting point, but they are born dT seconds after each other where $dT = 30{,}000/\int q_{tot} dV$ ($\int q_{tot} dV$ = the total production rate of ENAs in our whole simulation box; compare (7)). The distance L between the ENAs on the trajectory is thus equal to $|V_i|\ dT$. The number of ENAs, dN_i, which are on the trajectory inside the cylinder of volume dV (= $dxdA$) is equal to $|s|/L$. Here s is the vector from the point P_{in} to the point P_{out}. This can be written in the form $dN_i = (dx/dT)\ (1/|V_{xi}|)$ because $|s_x| / |s| = dx / |s| = |V_{xi}|\ \Delta T / |V_i|\ \Delta T| = |V_{xi}| / |V_i|$. Here ΔT is the time it takes for an ENA to move through the cylinder from the point P_{in} to the point P_{out}.

The ENA particle density (n_{ENA}), the bulk velocity (U_{ENA}), and the particle flux (J_{ENA}) inside the cylinder is therefore

$$n_{ENA} = (\sum_i dN_i) / dxdA = \frac{1}{dTdA} \sum_i \frac{1}{|V_{xi}|}, \tag{9a}$$

$$U_{ENA} = (\sum_i dN_i V_i) / dxdA = \left[\frac{1}{\sum_i |V_{xi}|^{-1}} \right] \sum_i \frac{V_i}{|V_{xi}|}, \tag{9b}$$

$$J_{ENA} = n_{ENA} U_{ENA}. \tag{9c}$$

Here dN_i is the number of ENAs within the cylinder of volume dV (=$dxdA$) on the trajectory i, V_i is the velocity of ENAs on that trajectory, and the sum is over all trajectories which go through the area dA.

The differential flux $j(\theta,\varphi)$ (cm^{-2} s^{-1} sr^{-1}) and omnidirectional flux $J(E)$ (cm^{-2} s^{-1} keV^{-1}) were calculated from the expressions:

$$j(\theta,\varphi) = \frac{1}{dAdTd\Omega} \sum_i \frac{1}{|\cos(\theta_i)|}, \tag{10}$$

$$J(E) = \frac{1}{dAdTdE} \sum_i \frac{1}{|\cos(\theta_i)|}. \tag{11}$$

Here θ_i is the (polar) angle between the ENA velocity vector V_i and the area vector $dA = -\ dA\ \mathbf{i}$ ($\mathbf{i}$ is the unit vector; compare Figure 4), φ is the azimuth angle, E is the energy of an ENA, and $d\Omega$ is the solid angle. The sum is over all trajectories i which penetrate the area dA. The cosine term arises because $dA|\cos(\theta_i)|$ is the area perpendicular to the ENA paths which have a velocity V_i.

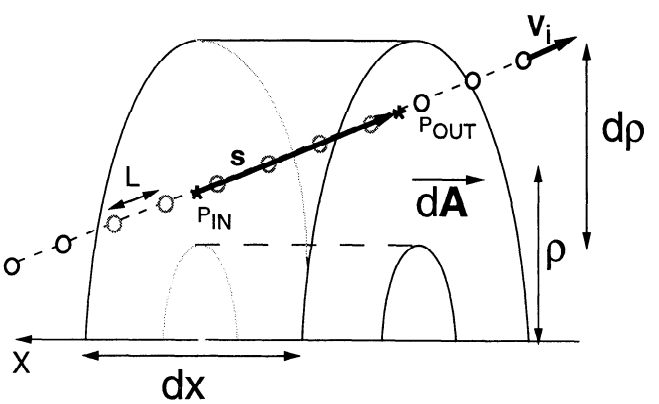

Figure 4. Illustration of the method used to calculate macroscopic parameters (not in scale). The dashed line shows a trajectory i, which penetrates a cylinder of height dx and the surface area dA. The distance of the ENAs (open circles) on the trajectory is L, and the velocity of ENAs on the trajectory is $\mathbf{V}_i$.

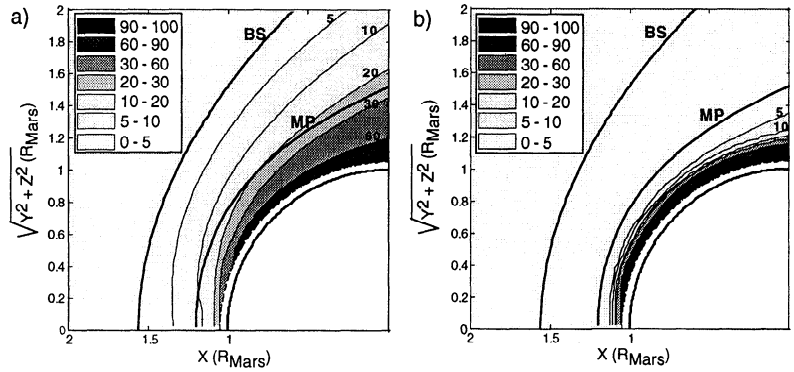

Figure 5. Percent of the absorbed solar wind protons for (a) solar minimum and (b) solar maximum EUV conditions. The bow shock (BS) and the magnetopause (MP) are showed by thick lines. The height of the obstacle boundary through which the protons can not flow is 170 km above the surface of Mars.

3. Loss of the Solar Wind Protons

3.1. Absorption

Figure 5 shows what percent of solar wind protons are absorbed by charge exchange with atomic and molecular hydrogen and oxygen during solar minimum (EUV1 model) and solar maximum (EUV3 model) when the magnetosphere is cold (T_{MPcold} model). The value displayed is $100(1 - \xi_H\xi_O\xi_{H2})$, where the ξ values are the exponential terms in (6).

For both solar minimum (Figure 5a) and solar maximum (Figure 5b), nearly all of the solar wind protons are absorbed above the obstacle boundary near the planet. This happens because the density of atmospheric neutrals is highest near the planet. Note that a few tens of percent of the solar wind protons are absorbed near the magnetopause boundary during solar minimum and only a few percent during solar maximum. In fact, no dramatic changes occur near the magnetopause because in this model the streamlines simply penetrate the magnetopause. According to our model, the magnetopause is not a place where the ion composition changes rapidly due to the charge exchange process. It should be noted that the absorption values at the bow shock are ≈ 3% for solar minimum and ≈ 1% in solar maximum.

3.2. Loss Rate

Figure 6 shows the relative solar wind loss rate for different atmospheric components, q_i/q_{tot}, for H, H_2, and O in the case where the energy dependence of the cross sections is disregarded. In this case the relative production rates depend on the height from the surface only and not on the velocity model (compare (3)). Note that a constant cross section is a good approximation for H and O but not for H_2, as seen in Figure 3. In fact, Figure 6 illustrates the importance of the different atmospheric components because the results presented below did not differ notably from the calculation where we used constant cross sections for H and O and disregarded H_2. Note in Figure 6 that during solar minimum (EUV1 model) the solar wind protons below ≈ 300 km altitude are lost mainly due to charge exchange with thermal oxygen. Oxygen therefore plays an important role at the "bottom" of the magnetosphere. Above it the hydrogen corona becomes more important. During solar maximum (EUV3 model), oxygen is an important constituent for higher altitudes as well.

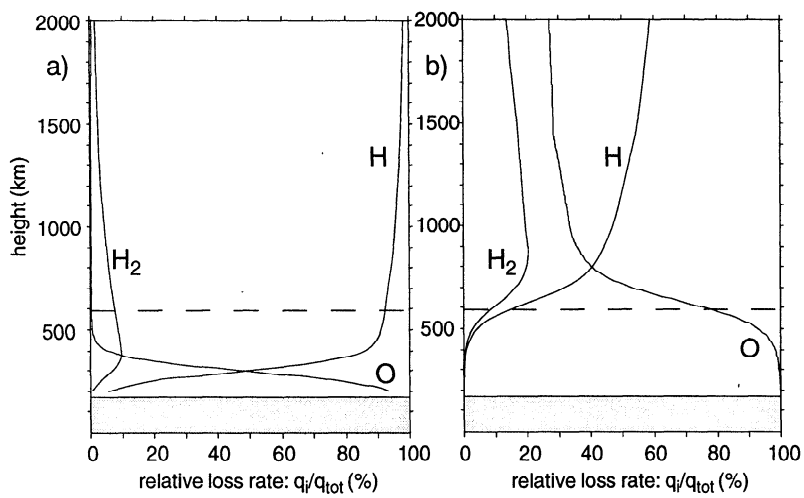

Figure 6. Estimation of the role of the H, H_2, and O atmospheres for the loss rate of solar wind protons. The relative production rates (= q_i/q_{tot}) is shown in percent in (a) solar minimum, and (b) solar maximum when the energy dependent cross sections were approximated by constants: $\sigma_H = 2\times10^{-15}$ cm^2, $\sigma_{H2} = 10^{-16}$ cm^2, and $\sigma_O = 10^{-15}$ cm^2. The shaded area at the bottom shows the region within the obstacle boundary of the velocity model. The dashed line shows the height of the magnetopause at SZA = 0°.

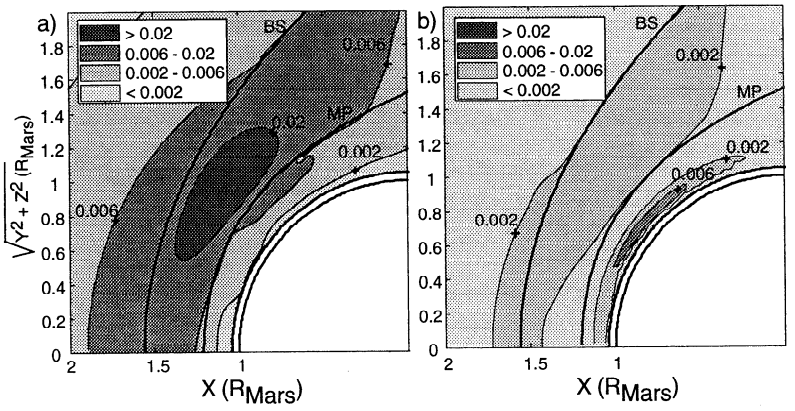

Figure 7. The loss rates ($cm^{-3}\,s^{-1}$) of solar wind protons due to charge exchange between the solar wind and Martian H, H_2, and O atmospheres. Loss rates are shown for (a) solar minimum and (b) solar maximum. The bow shock (BS) and the magnetopause (MP) are showed by thick lines and no ENAs are assumed to penetrate the obstacle boundary (thick circle around Mars).

Atomic hydrogen is the most important constituent in the magnetosheath and in the solar wind. In reality the cross sections and thus the relative loss rate vary on the (x, ρ) plane, and we used energy dependent cross sections in our calculations below.

Figure 7 shows the loss rate of solar wind protons calculated from (3) for solar minimum (EUV1 model) and solar maximum (EUV3 model) EUV conditions when the magnetosphere is cold (T_{MPcold} model). Two different regions where the loss rate is high are seen: the magnetosheath at solar minimum (Figure 7a) and the magnetosphere at solar maximum (Figure 7b).

The reason for high loss rates in these two regions is different. The magnetosheath is a region of high solar wind fluxes but tenuous neutral atmosphere. The magnetosphere instead is a region of relatively dense neutral atmosphere but small solar wind fluxes. During solar minimum the highest loss rates are obtained in the magnetosheath where the absorption is mainly due to the hydrogen exosphere (compare Figure 6a). For solar maximum, in contrast, the highest loss rates are obtained near the inner surface boundary inside in the magnetosphere. At these low altitudes the protons are absorbed mainly by thermal oxygen (compare Figure 6b). Note that the loss rate in the magnetosheath decreases at solar maximum because the density of the hydrogen exosphere decreases. This is opposite to the behavior of oxygen for which the density increases with increasing solar activity (compare Figure 2).

It should be noted that the maximum loss rate in the magnetosheath and in the magnetosphere lies around SZA ≈ 45° and not above the subsolar point. The reason for this is the fact that the particle flux near the stagnation point is low (compare Figure 1d). In the magnetosheath the maximum loss rate occurs at higher SZA because the proton flux increases with increasing SZA while the density of atmospheric neutrals decreases only slightly along the streamlines with increasing SZA. In the dayside magnetosphere the loss is greatest at higher SZAs where the proton flux is maximum.

4. Energetic Neutral Atoms Near Mars

4.1. ENA Environment

Figure 7 also shows the production rate of ENAs because the ENA production rate is the same as the loss rate of the solar wind protons. Therefore there are two different ENA source regions downstream of the bow shock: the magnetosheath and the magnetosphere. Moreover, these ENAs have characteristics which differ from the characteristics of ENAs born in the solar wind upstream of the bow shock. Those ENAs create the third ENA population.

Figure 8 shows where the ENAs move from the three different source regions. In both figures the launching points are on the *XZ* plane. These ENA trajectories near Mars illustrate how the ENA's motions depend on the proton streamlines and on the proton temperature in the different plasma regions around Mars. Some of the starting points were placed in the solar wind, some in the magnetosheath, and part in the magnetosphere. Figure 8a shows the case where the plasma temperature is set to 0. The direction of the velocity vector of an ENA is thus a tangent to the streamline at the point where the ENA was born. The undisturbed solar wind flows along the -*X* axis, and therefore the trajectory of an ENA born in the solar wind is a straight line parallel to the *X* axis. Mars, or more precisely, its atmosphere, absorbs part of these ENAs. Note that the trajectories of ENAs born in the magnetosheath are concentrated in the magnetosheath. ENAs born in the magnetosphere instead are more spread around into the whole space.

Figure 8b shows ENA trajectories initiated at the same positions as the ENAs shown in Figure 8a for the cold temperature model (T_{MPcold} model) when the assumed proton temperature in the solar wind was 13 eV and the solar wind velocity 400 km s^{-1}. Because of the thermal spread, the trajectories are no longer on the *XZ* plane as in the zero temperature model. Note that the directions of the new trajectories do not differ markedly from the previous trajectories in the solar wind, and in the magnetosheath away from the subsolar point, where the bulk flow is high. However, the thermal velocity component is comparable to or even much larger that the bulk velocity in the subsonic region in the magnetosheath near the *X* axis and especially in the magnetosphere. In Figure 8b these regions are like an ENA point source where atoms are spread over all (4π) angles. Many of the ENAs born in the magnetosphere are therefore likely to impact the planetary obstacle in this case. The circles near the planet show the positions where ENAs hit the planetary obstacle. It should finally be noted that the parameter which determines the thermal speed

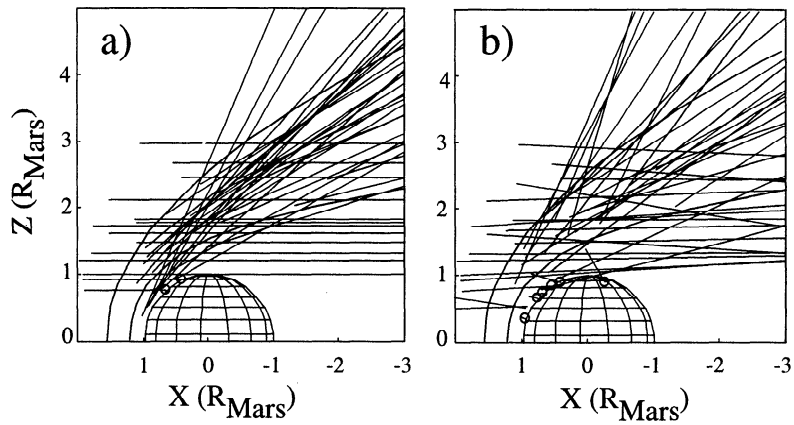

Figure 8. Examples of ENA trajectories around Mars. (a) Trajectories when the proton temperature is put to 0. (b) Trajectories starting from the same positions on the *XZ* plane as Figure 8a when the temperature in the solar wind is 13 eV and downstream of the bow shock half of the gas dynamic temperature. The circles near the planet show the positions where ENAs hit the planetary obstacle.

of ENAs at a given position is the sonic Mach number at that point. The sonic Mach number determines how strongly the direction of the velocity vector of an ENA differs from the direction of the streamline at the point where the ENA is born because of the thermal spread.

Figure 9 shows the spatial distribution of the ENA particle flux |J| calculated from (9c) and displays flux contours of ENAs near Mars for solar minimum (EUV1 model) and solar maximum (EUV3 model) for a cold temperature model (T_{MPcold} model). In Figure 9 the proton temperature in the solar wind was put to 0 to simplify the calculations. In Figures 9a and 9b, U_{SW} = 400 km s^{-1}, n_{SW} = 2.5 cm^{-3}, and T_{SW} = 13 eV.

For solar minimum the ENA flux maximum is in the magnetosheath. This is because the production rate is highest in the magnetosheath (compare Figure 7a) and because ENAs born in the magnetosheath remain in the magnetosheath a long time (compare orbits in Figure 8b). A very sharp shadow behind Mars is formed because the temperature in the solar wind is assumed to be 0. In reality, the shadow boundary is more gradual because of the thermal spread and because some ENAs which move close to the planet will be absorbed by the Martian atmosphere (see Appendix). Note that at solar maximum there are two local flux maxima. The new region of high ENA fluxes in the magnetosphere is formed because the production rate increases near the obstacle surface (compare Figure 7b).

In Figure 9 the proton integral flux was 10^8 cm^{-2} s^{-1} and therefore the maximum ENA fluxes are a few percent of the solar wind flux. Near the bow shock, for example, the ENA fluxes are ≈ 3% and <≈1% for solar minimum and maximum conditions, respectively. These values are close to the absorption values near the bow shock (compare Figure 5), indicating that the amount of ENAs in the solar wind which are born downstream of the bow shock is relatively small. An exception is the nose region where there are a remarkable amount of ENAs born in the highly subsonic region.

Figure 10 shows the ENA energy spectra, *J(E)*, calculated from (11). These represent what could be seen by an omnidirectional ENA instrument with no directional resolution during solar minimum (EUV1 model). Results for two different magnetosphere temperature models are included. The energy spectra were calculated for five locations shown in Figure 10a: 1, the nightside magnetosheath; 2, the nightside magnetosphere; 3, the dayside magnetosphere; 4, the dayside magnetosheath; and 5, the solar wind. Figure 10b shows the energy spectra for the cold temperature model (T_{MPcold} model) where the proton temperature in the magnetosphere can be less than 1 eV. Figure 10c shows the hot temperature model (T_{MPhot} model) where the proton temperature in the magnetosphere is typically over 100 eV. The solar wind parameters are the same as used in Figure 9. Note, however, that Figure 10 also shows the energy spectra of ENAs born upstream of the bow shock when the proton temperature is 13 eV, that is, not 0.

The ENA populations at different observation points are composed of remotely produced ENAs which can reach these

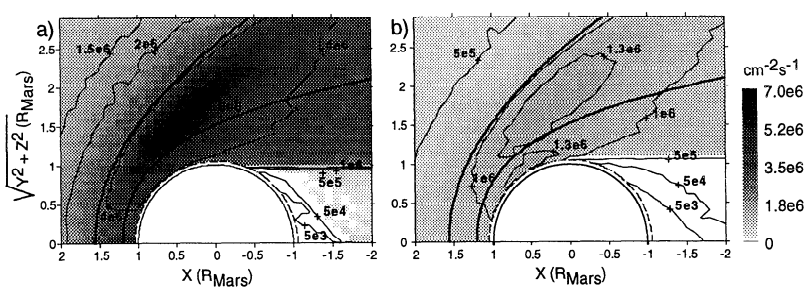

Figure 9. ENA fluxes |J| around Mars for (a) solar minimum and (b) solar maximum conditions. In both cases the solar wind flux was 10^8 cm^{-2} s^{-1}. The bow shock and the magnetopause are shown by thick lines, and the obstacle boundary is shown by the dashed circle. Read 1.5e6 as 1.5×10^6

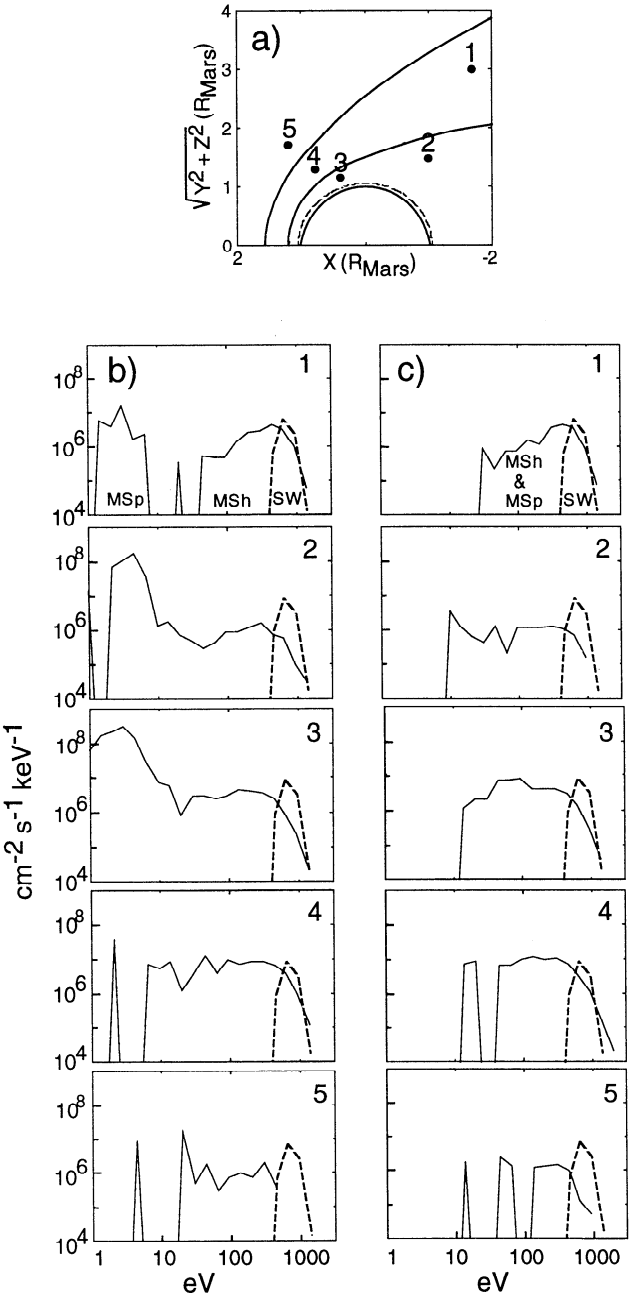

Figure 10. (a) The positions where the five ENA energy spectra are collected. ENA energy spectra for the (b) cold and (c) hot magnetosphere temperature models for solar minimum. In both cases the dashed lines show the ENAs born upstream of the bow shock, and the solid lines show the ENAs born downstream of the bow shock. Note that the ENAs born in the magnetosphere (Msp) can be distinguished from the ENAs born in the solar wind (SW) and in the magnetosheath (Msh).

points. In general, three ENA populations can be identified in Figure 10: ENAs produced in the solar wind, the magnetosheath and the magnetosphere. They are characterized by different values of bulk velocities and temperatures reflecting different plasma parameters in the remote generation regions. Note that these three ENA populations come also from different directions (compare Figure 8). It should be noted that we can distinguish ENAs produced in different regions because our ENA simulation is a test particle simulation and therefore we automatically know the origin of the ENA which was detected in a given point in our model.

The ENAs produced in the solar wind result in a narrow flux peak (up to 10^7 cm^{-2} s^{-1} keV^{-1}) at the typical solar wind energy of 850 eV (<-> 400 km s^{-1} for protons). The ENAs from the magnetosheath form a hot component with a rather hard spectrum within 50-1000 eV and a flux up to 10^7 cm^{-2} s^{-1} keV^{-1}. For the cold magnetosphere model the highest ENA flux up to 3×10^8 cm^{-2} s^{-1} keV^{-1} is observed in the magnetosphere below 10 eV. These low-energy ENAs produced in the magnetosphere are clearly separated from the ENAs born in the magnetosheath or in the solar wind. Note that the differential flux of the magnetospheric ENAs is not so intense in the hot as in the cold magnetosphere model because the thermal spreading is significantly higher in the former case. Note also that the hot magnetospheric ENAs are mixed up with ENAs from the magnetosheath.

Important new information about the interaction regions can be inferred from the ENA directional distribution. Figure 11 shows the ENA integral flux $j(\varphi, \theta)$ (cm^{-2} s^{-1} sr^{-1}) calculated from (10) at the first four positions (1, 2, 3, 4) shown in Figure 10a. Shown in Figure 11 are mercator projections of ENA differential fluxes, so-called ENA images, as they would be seen by a direction-sensitive ENA instrument with no energy resolution. The ENA fluxes are displayed as a function of two spherical angles, azimuth(φ) and polar angle(θ). For every point the spherical coordinate system was chosen with the Z' (polar) axis pointing toward the center of Mars. The X' axis is in the plane which contains the X axis of the model and the observational point and points to the $+X$ direction. In these coordinates the Sun is always at the azimuth angle of 180°, and the center of Mars is at the polar angle of 0°.

Figure 11, as well as Figure 10b, shows the ENA "image" for the solar minimum conditions (EUV1 model) when the magnetosphere is cold (T_{MPcold} model) and when the solar wind velocity is 400 km s^{-1}, the solar wind flux 10^8 cm^{-2} s^{-1}, and the solar wind temperature 13 eV. In our model the solar wind bulk velocity has only an x component, and thus the ENAs born in the solar wind are concentrated around solar directions. These ENAs present the highest flux > 10^7 cm^{-2} s^{-1} sr^{-1}. The second local maximum seen in Figures 11a and 11c are produced by ENAs originating in the magnetosheath and the magnetosphere. Closer to the planet these ENAs occupy a wider range of azimuthal angles because the plasma velocity decreases and the relative temperature spreading increases. Note that if one has taken the plasma temperature to be 0 everywhere, the azimuthal spreading would disappear and the ENA images would look like a line at the 180° azimuth. The chosen model is axially symmetric, and therefore the width of the angular distribution obtained depends on the plasma temperature only.

4.2. Atmospheric Effects of Precipitating ENAs

ENAs transfer part of the solar wind bulk energy and particles directly into the Martian atmosphere when they hit the atmosphere. During solar minimum and maximum the flux of ENAs born upstream of the bow shock is about 3% and 1% of the solar wind particle flux, respectively, as pointed out in section 3.1. These ENAs move predominantly toward the $-X$ direction and hit the Martian upper atmosphere. For the solar wind flux used in our simulation of 10^8 cm^{-2} s^{-1}, about 10^{24} and 3.6×10^{23} hydrogen atoms hit the Martian atmosphere per second for solar minimum and solar maximum conditions, respectively. Moreover, for the assumed solar wind velocity of 400 km s^{-1}, 3%

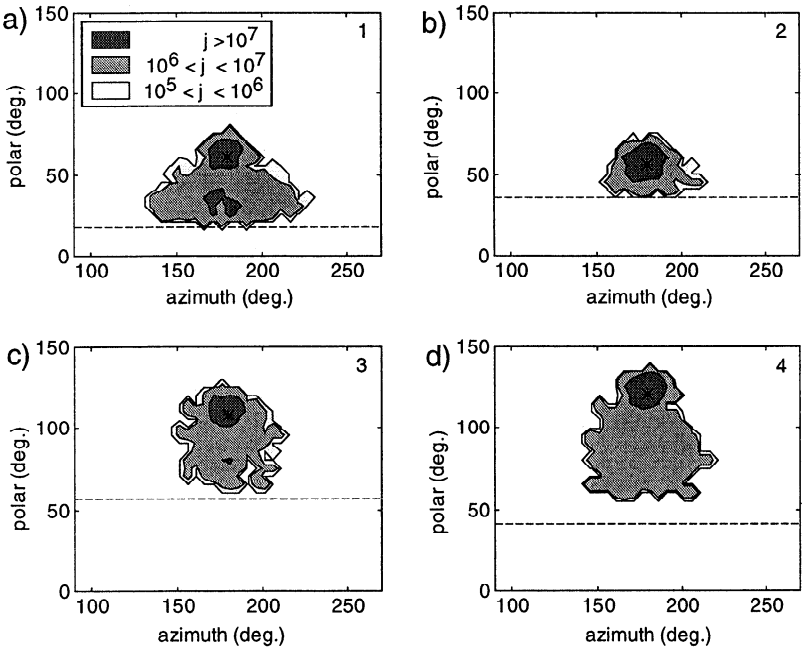

Figure 11. The ENA integral flux (cm^{-2} s^{-1} sr^{-1}) at the first four positions shown in Figure 10a in the solar minimum conditions as a function of two spherical angles, azimuth and polar angle. The star shows the position of the Sun, and the dashed line shows the limb of Mars.

and 1% correspond to an energy flux of about 2.6×10^9 eV cm^{-2} s^{-1} at solar minimum and 8.5×10^8 eV cm^{-2} s^{-1} at solar maximum. These numbers correspond to ENAs born upstream of the bow shock and do not include ENAs produced in the magnetosheath and magnetosphere which can also hit the upper atmosphere (see Figure 8b; the circles mark the impacting ENA trajectories).

The precipitating ENAs can affect the Martian ionosphere aeronomy, because they present an extra source of energy. In order to illustrate the importance of this source we compare it with others: the precipitating O^+ pickup ions, solar wind proton absorption, and solar EUV. Figure 12 shows the energy flux supplied by these sources. The energy flux of precipitating O^+ and H^+ ions was calculated by using the solar wind parameters U_{SW} = 400 km s^{-1}, M_{sonic} = 4.5 [*Luhmann and Kozyra*, 1991], and U_{SW} = 425 km s^{-1}, n_{SW} = 2 cm^{-3} [*Brecht*, 1997], respectively. The ENA energy flux was calculated for U_{SW} = 400 km s^{-1} and n_{SW} = 2.5 cm^{-3}.

Figure 12 suggests that ENA precipitation can be an important energy source in the Martian ionosphere. For example, the energy flux averaged over the dayside associated with the O^+ ions is only 6×10^7 eV cm^{-2} s^{-1} according to a test particle simulation based on a gas dynamic model [*Luhmann and Kozyra*, 1991]. These ions are produced in the Martian oxygen corona outside the obstacle where they are picked up by the solar wind and can impact the dayside atmosphere. The similar effect of the finite solar wind proton gyroradius in the Martian magnetosheath was estimated from a hybrid simulation [*Brecht*, 1997]. Some of the solar wind protons impact the obstacle when Mars like scaling and interplanetary parameters are used. The energy flux depends on the longitude and latitude and varies within 10^7 - 10^8 eV cm^{-2} s^{-1}, with the relatively localized flux peak reaching 10^9 eV cm^{-2} s^{-1}.

Figure 12 also compares the energy flux deposited by the ENAs with the heating resulting from the solar radiation absorption. Altitude integrated total heating rate due to the solar radiation for the altitude range 100 - 240 km is ≈ 1.35×10^{11} eV cm^{-2} s^{-1} (derived from *Fox and Dalgarno* [1979, Figure 14, model B profile]). This value is based on the conditions at the time of the entry of Viking, that is, on solar minimum conditions at SZA 45°. A substantial part of this heat is carried by the neutral products, although ≈3.54×10^9 eV cm^{-2} s^{-1} is deposited as kinetic

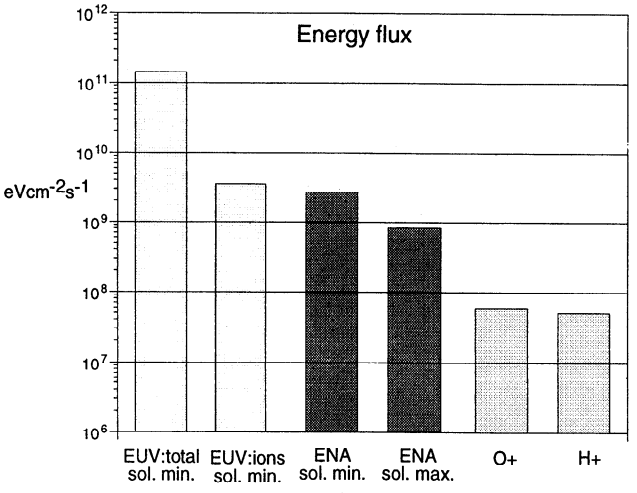

Figure 12. The relative importance of different heat sources in the Martian ionosphere. The first and second bars show the energy of the total heating due to the solar radiation absorption and the heat deposited as kinetic energy of ions during solar minimum, respectively [from *Fox and Dalgarno*, 1979]. The third and forth bars show the ENA energy precipitation flux for solar minimum and maximum based on this study. The fifth and sixth bars show the energy flux supplied by the precipitating O^+ ions [from *Luhmann and Kozyra*, 1991] and H^+ ions [from *Brecht*, 1997].

energy of ions (derived from the altitude profile of *Fox and Dalgarno* [1979, in Figure 17]). Figure 12 shows the total heating due to the solar radiation absorption and the heat deposited as kinetic energy of ions. The latter is very close to the energy deposited by ENA which indicates that ENA may cause heating effects in the Martian upper atmosphere, although a detailed aeronomic analysis of the ENA precipitation is needed. It should be noted that the energy flux deposited by ENAs grows almost as the third power of the solar wind velocity since the charge exchange cross section depends only slightly on the energy. Therefore temporal variations in the solar wind may cause significant increase of the energy flux deposited by the ENA precipitation and hence heating rates in the Martian upper atmosphere.

In addition to heating, the precipitating ENAs may also affect the atmospheric ion composition. For the region upstream of the bow shock the most important atmospheric constituent for the charge exchange process is hydrogen (compare Figure 6). A charge exchange reaction between an exospheric hydrogen atom and a solar wind proton resulting in a precipitating ENA does not change the amount of hydrogen in the exosphere. This process, which can be called hydrogen recycling, only replaces a planetary hydrogen atom with a hydrogen atom from the solar wind. In order to illustrate the relative rate of the hydrogen recycling, one can compare it with the total ($H+2H_2$) hydrogen thermal escape rate, 3.6×10^{26} s^{-1}, which corresponds to the escape flux of 2.5×10^{8} cm^{-2} s^{-1} obtained from a one-dimensional photochemical model of the Martian atmosphere [*Krasnopolsky*, 1993]. This escape rate is therefore much higher than the rate at which the hydrogen atoms in the Martian atmosphere are replaced by ENAs (10^{24} s^{-1} at solar minimum).

5. Discussion

We have studied several effects of the charge exchange process between the solar wind protons and the Martian neutral upper atmosphere by using an empirical proton flow model. It is important to realize how the results depend on the features of the global model in order to understand the similarities and differences of our results compared to earlier results based on different global models.

There are three important parameters of the adopted velocity model: the streamlines, the plasma velocity and the temperature. The streamlines, together with the neutral upper atmospheres, determine what percent of the solar wind protons are absorbed, if the charge exchange cross sections do not depend strongly on the energy (compare (6)). In the empirical model the streamlines which are depleted of protons near the inner obstacle surface also remain near the surface on the dayside. The absorption region is thus a thin layer above the obstacle boundary, which in our model was a sphere of 170 km above the surface of Mars.

This absorption layer resembles the results obtained earlier by *Gombosi et al.* [1981] and *Russell et al.* [1983] who studied the absorption of the solar wind protons by the Venusian and Martian atmospheres, respectively. In both studies the authors used streamlines which approximated the GD streamlines. The important feature is that their ionopause was a sphere of 200 km above the surface of the planet, much like the obstacle boundary in our empirical model. Therefore their streamlines look much like the streamlines in our empirical model, resulting in a thin absorption layer above the surface. However, a gas dynamic model, where the Newtonian pressure balance equation is used to create an ionopause, gives quite different streamlines. In this case the ionopause is a blunt surface above the planet, which is much closer to the surface near the subsolar point than at the terminator. Therefore the streamlines, which are depleted of protons near the subsolar point, move to higher altitudes with increasing SZA, giving high absorption rates at high altitudes. These streamlines were used by *Ip et al.* [1994] and *Lichtenegger et al.* [1997].

The second consequence of the shape of the blunt ionopause is that if the nose of the ionopause is in the region where the thermal oxygen dominates, the maximum absorption is obtained near the X axis in contrast to our results. This is because the scale height of the thermal oxygen is so small that increasing the altitude of the ionopause decreases the density of the available atmosphere markedly. Therefore the absorption rate decreases rapidly with increasing SZA. However, we do not know how high the "magnetopause" or the "ionopause" at the subsolar point at Mars really is. In earlier works the height of the ionopause at the subsolar point was assumed to be 300 km [*Ip et al.*, 1994; *Lichtenegger et al.*, 1997]. In our empirical model the magnetopause is 600 km above the surface at the subsolar point where the neutral scale height is much larger than at 300 km. Given these differences, *Ip et al.* [1994] got much higher absorption rates at high altitudes than what we obtained with our empirical model. For the same reasons, *Lichtenegger et al.* [1997] obtained a loss rate maximum near the subsolar point.

When we study the observed decrease of the proton flux using gas dynamic models, it is important to recall that the streamlines alone determine the proton fluxes if there are no proton sinks or sources. In the empirical model the proton flux decreases at the magnetopause, but as a consequence of the geometry of the model streamlines. No losses are needed to produce a magnetosphere where the proton flux is smaller than in the magnetosheath (compare Figure 1d). In fact, in our model the absorption rate near the magnetopause on the dayside is a few tens of percent for solar minimum and only a few percents for solar maximum. Therefore, according to the empirical model, the observed decrease of the solar wind flux near the magnetopause [see *Lundin et al.*, 1991] cannot be a result of the charge exchange process. It should also be noted that *Lichtenegger et al.* [1997] obtained about a 100 times larger loss rate than is obtained here mainly because in our model the proton flux in the magnetosphere can be about 100 times less than in the solar wind.

A notable feature of ENAs is that they give information about the global features of the Mars-solar wind interaction because ENA properties are related to the flow geometry, the proton velocity, and the proton temperature. The streamline geometry determines the direction of the bulk velocity and thus affects the direction of ENA trajectories. The ratio of the proton bulk velocity and the thermal velocity, the sonic Mach number, determines how strongly the velocity of a newly born ENA differs from the direction of the streamline. Our results illustrate that the energy distribution of ENAs can include several peaks which correspond to various source regions with different bulk velocities and temperatures. For example, the ENAs originating in the magnetosheath and the magnetosphere (compare Figure 11) produce distinctive structure on the ENA images, because these most intense ENA production regions are defined by different plasma and the neutral gas distributions at these locations. Therefore ENAs are a probe of the near-Mars plasma properties giving information about the direction of the proton flow, about the strength of the transfer of bulk energy of the solar wind protons into thermal energy, and about the density of the neutral upper atmospheres.

The effect of the fraction of the ENAs entering the deeper atmosphere of Mars is unknown. However, our comparison of the three heat sources related to the plasma physical processes, namely, ENA, O^+ ion, and solar wind H^+ precipitation, suggest that the ENA precipitation is the most important one. It should be noted that the Martian ionospheric models which start with the observed neutral atmosphere exposed only to the solar radiation do not reproduce the observed ion and electron temperature profiles (see discussions of *Luhmann and Kozyra* [1991, and references therein]). To reproduce observations, the models have to include both horizontal magnetic field to limit heat conductivity and heat sources at the ionospheric boundaries. These extra heat sources have generally been attributed to the solar wind, although the mechanisms for such heating were not well understood. The precipitating ENA directly linking the solar wind and the ionosphere/upper atmosphere might present such a mechanism. However, a specific aeronomical study needs to performed in order to describe the energy transfer from the precipitating hydrogen to the atmosphere in detail. From the atmospheric composition point of view it is finally interesting to note that the solar wind contains essentially no deuterium: the upper limit of the ratio $(D/H)_{solar\ wind}$ is $< 3\times10^{-6}$ [*Geiss and Reeves*, 1972]. In contrast, the abundance of deuterium on Mars is rather high $(D/H)_{Mars} = (9\pm4)\times10^{-4}$ [*Owen et al.*, 1988]. Therefore it would be interesting to determine whether the hydrogen recycling affects the isotopic abundance of hydrogen on Mars over the timescales of planetary evolution.

Finally, we would like to emphasize that many assumptions have been made which limit our results. First, we used a model of the proton flow that is axially symmetric. In practice, for example, the magnetic field [see *Tanaka*, 1993], kinetic effects [see *Brecht and Ferrante*, 1991], and the mass loading can create asymmetric features in the flow. Therefore the real ENA environment is expected to have asymmetric features. Moreover, we always used the same shape and altitude for the bow shock, the magnetopause, and the obstacle boundary, while these in fact change with the solar wind parameters. We also assumed that the proton distribution function is Maxwellian everywhere. There are also instrumental constraints limiting the possibility to detect the ENAs under discussion. For example, ENAs with typical energy less than 10 eV (compare Figure 10b) could be hardly measured using modern ENA instruments. In addition, the ENA flux produced in the solar wind is superimposed on the solar photon radiation flux to which ENA detectors are usually rather sensitive at EUV wavelengths [see, e.g., *Barabash et al.*, 1995]. However, the calculated ENA integral fluxes are very high ($\geq\approx 10^7$ cm^{-2} s^{-1} sr^{-1}), much higher than those expected in the Earth environment [*Hesse et al.*, 1993; *Moore et al.*, 1994] which makes Mars a very attractive target to be studied by means of ENA imaging techniques (see review of *Williams et al.* [1992]).

6. Summary

We have studied some of the consequences of the charge exchange between solar wind protons and Martian atomic and molecular hydrogen and oxygen atmospheres and how the results depend on solar activity and the near-Mars plasma behavior. The solar wind, the magnetosheath and the magnetosphere were found to be three distinct regions from the charge exchange process point of view. The solar wind and the magnetosheath are regions of high solar wind fluxes but tenuous neutral atmosphere. ENAs born in the solar wind form a cold ENA population moving predominantly antisunward. These ENAs are produced mainly from the extended Martian atomic hydrogen atmosphere, and they can precipitate into the Martian upper atmosphere, depositing energy. Around solar minimum the absorption of solar wind in the magnetosheath is mainly by the atomic hydrogen exosphere, while at solar maximum the oxygen and the molecular hydrogen become important as well. The ENA flux in the magnetosheath is very high and reaches 10^7 cm^{-2} s^{-1} keV^{-1} within the energy range 0.05 - 1 keV.

The magnetosphere, instead, is a region of denser neutral atmosphere, but smaller solar wind fluxes. For solar minimum conditions, the oxygen contributes to the solar wind loss and hence to the ENA production primarily near the planet. For solar maximum the oxygen is important throughout the magnetosphere at small solar zenith angles. The thermal oxygen causes an intensive absorption of the solar wind protons in the magnetosphere near the planetary obstacle surface. Mass loading effects are expected to be most important in this region. The amount of absorption of solar wind protons near the magnetopause is too small to cause the observed decrease of the solar wind protons. If the proton temperature in the magnetosphere is much lower than in the magnetosheath, ENAs born in the magnetosheath create a cold component in the ENA energy spectra (< 10 eV) which can be distinguished from the hot ENA component. Although ENA detectors are not currently a part of any planned Mars mission, the model results presented here suggest their value as a unique information source for understanding the space environment of Mars including the global proton flow geometry, the proton speed and the proton temperature.

Appendix: Loss of ENAs

All above calculations of the ENA production were performed under the assumption that the medium near Mars is optically thin (more correctly, "ENA" thin), that is, the attenuation of the ENA flux, wherever it occurs, is negligible. In order to justify this assumption we have carried out calculations of the ENA beam attenuation due to interaction with the Martian exosphere. The attenuation occurs when a fast hydrogen atom interacts with the same neutral components as those which produce ENAs, namely, atomic and molecular hydrogen, oxygen, and helium. In our calculation we included two destructive reactions, stripping and electron detachment (except for H on O for which the detachment cross section is unknown). The former gives rise to converting fast hydrogen atoms into positive ions which are then picked up by the solar wind and the latter results in negative ion formation. For the molecular hydrogen we took into account the ionization reaction $H + H_2 \rightarrow H + H_2^+ + e$ as well, because it causes the hydrogen atom to lose directional information. The different types of excitations were not considered and neither were dissociative collisions between hydrogen and molecular hydrogen because the cross section for this reaction is typically less than 10^{-19} cm^2. The total cross section numbers for the H, He, and H_2 gases were taken from the compilation by *Barnett* [1990], and the stripping cross section for oxygen was taken from *Basu et al.* [1987]. All cross sections in question decrease with energy in the range 0.001 - 1 keV. Thus for our maximum attenuation calculations we can simply choose the maximum cross section corresponding to 1 keV and assume it constant. The following cross sections, σ^{lost}, were used:

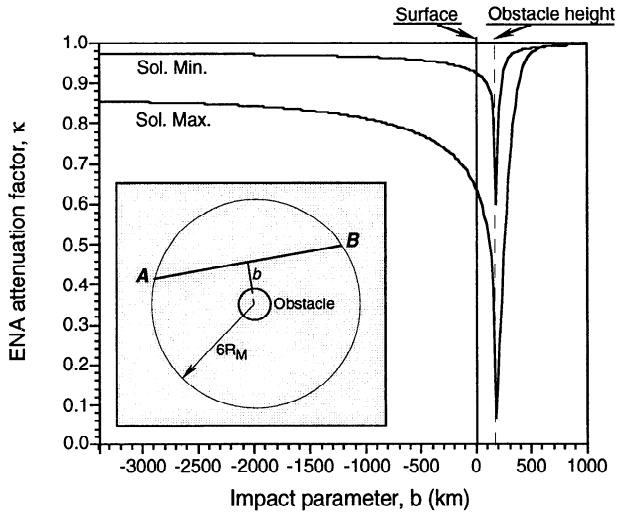

Figure A1. The ENA beam attenuation factor κ as a function of the impact parameter b for the solar maximum and minimum conditions. If κ = 1 there is no absorption of ENAs, while κ = 0 means that all ENAs are absorbed into the Martian atmosphere. The insert shows the integration path AB, the planet and the obstacle boundary (the thin circle around Mars). The ENAs were assumed to be born at the sphere of the radius $6R_{Mars}$.

$$\begin{aligned} &H + H: \quad \sigma_H^{lost} = 1.62\times10^{-18}\ cm^2, \\ &H + H_2: \quad \sigma_{H2}^{lost} = 4.05\times10^{-17} cm^2, \\ &H + O: \quad \sigma_O^{lost} = 1.0\times10^{-16}\ cm^2, \\ &H + He: \quad \sigma_{He}^{lost} = 3.33\times10^{-17}\ cm^2. \end{aligned} \tag{A1}$$

The attenuation factor κ was calculated according to the formula similar to (6):

$$\kappa = e^{-\sum_{k=1}^{4} \sigma_k^{lost} \int_A^B n_k(l)\,dl} \tag{A2}$$

However, now the integrations were performed along straight lines inside the sphere of radius $6R_{Mars}$ (see the insert in Figure A1). The index k runs over all neutral components, their density distributions, $n_k(l)$, along the integration lines are given by the Chamberlain formula [see, e.g., *Chamberlain and Hunten*, 1987]. The integration lines were parameterized by the impact parameter b. Positive b values correspond to trajectories outside the Martian surface, and negative b values correspond to those crossing the surface. If the line crosses the sphere of the radius (R_{Mars}+170)km (the obstacle boundary), the integration is performed only between the crossing point and the point on the external sphere.

Figure A1 gives the dependence of the attenuation factor κ on the impact parameter for solar minimum and solar maximum conditions. For solar minimum, only ENA beams passing over the planet within a very narrow range of impact parameters close to the obstacle boundary may experience attenuation up to 40% (i.e., κ = 0.6). For the trajectories which are 240 km from the Martian surface, the attenuation is less than 10%, that is, negligible. Thus for the solar minimum conditions the medium around Mars can be considered as ENA thin. Due to the significant increase of the oxygen density both in thermal and hot components, the ENA beam attenuation becomes significant at low altitude because of the low scale height of the oxygen. The attenuation is negligible for impact parameters greater than 380 km.

Finally, we would like to emphasize that these calculations give the maximum possible attenuation factors because we assumed that ENAs were born at the planetocentric distance $6R_{Mars}$ and used the maximum interaction cross sections. For ENAs traveling along specific trajectories, as shown in Figure 8, and less than 1 keV energy, the attenuation is much less. Moreover, the Martian exosphere densities are known with much less accuracy than the factors above.

Acknowledgments. The authors are very grateful to Rickard Lundin for initiating the studies of ENA at Mars. This work was partially supported by NASA grant NAGW-4600 and by the Academy of Finland.

The Editor thanks A. F. Nagy and S. W. Bougher for their assistance in evaluating this paper.

References

Barabash, S., R. Lundin, T. Zarnowiecki, and S. Grzedzielski, Diagnostic of energetic neutral particles at Mars by the ASPERA-C instrument for the Mars 96 mission, *Adv. Space Res., 16*, 81 - 86, 1995.

Barnett, C. F., Collisions of H, H_2, He and Li atoms and ions with atoms and molecules, in *Atomic Data for Fusion Ser.*, vol. 1, Rep. ORNL-6086, edited by H. T. Hunter et al., Oak Ridge Nat. Lab., Oak Ridge, Tenn., 1990.

Basu B., J. R. Lasperse, R. M. Robinson, R. R. Vondrak, and D. S. Evans, Linear transport theory of auroral proton precipitation: A comparison with observations, *J. Geophys. Res., 92*, 5920-5932, 1987.

Brecht, S. H., Solar wind proton deposition into the Martian atmosphere, *J. Geophys. Res., 102*, 11,287-11,297, 1997.

Brecht, S. H., and J. R. Ferrante, Global hybrid simulation of unmagnetized planets: Comparison of Venus and Mars, *J. Geophys. Res., 96*, 11,209-11,220, 1991.

Chamberlain, J. W., and D. M. Hunten, *Theory of Planetary Atmospheres*, 2nd ed., p. 335, Academic, San Diego, Calif., 1987.

Fox, J. L., and A. Dalgarno, Ionization, luminosity, and heating of the upper atmosphere of Mars, *J. Geophys. Res., 84*, 7315-7333, 1979.

Geiss, J., and H. Reeves, Cosmic and solar system abundances of deuterium and helium-3, *Astron. Astrophys., 18*, 126-132, 1972.

Gombosi, T. I., M. Horanyi, T. E. Cravens, A. F. Nagy, and C. T. Russell, The role of charge exchange in the solar wind absorption by Venus, *Geophys. Res. Lett., 8*, 1265-1268, 1981.

Hesse, M., M. F. Smith, F. Herrero, A. G. Ghielmetti, E. G. Shelley, P. Wurz, P. Bochsler, D. L. Gallagher, T. E. Moore, and T. S. Stephen, Imaging ion outflow in the high-latitude magnetosphere using low-energy neutral atoms, *Opt. Eng., 32*, 3153-3160, 1993.

Ip, W.-H., T. K. Breus, and T. Zarnowiecki, Termination of the solar wind proton flow near Mars by charge exchange, *Planet. Space Sci., 42*, 435-440, 1994.

Kallio, E., An empirical model of the solar wind flow around Mars, *J. Geophys. Res., 101*, 11,133-11,147, 1996.

Kallio, E., and H. Koskinen, Ion acceleration in the Martian plasma environment, *Adv. Space Res.*, in press, 1997.

Krasnopolsky, V. A., Solar cycle variations of the hydrogen escape rate and the CO mixing ration on Mars, *Icarus, 101*, 33-41, 1993.

Krasnopolsky, V. A., and G. R. Gladstone, Helium on Mars: EUVE and PHOBOS data and implications for Mars' evolution, *J. Geophys. Res., 101*, 15,765-15,772, 1996.

Lichtenegger, H., E. Dubinin, and W.-H. Ip, The depletion of the solar wind near Mars, *Adv. Space Res.*, in press, 1997.

Luhmann, J. G., and J. U. Kozyra, Dayside pickup oxygen ion precipitation at Venus and Mars: Spatial distributions, energy deposition and consequences, *J. Geophys. Res., 96*, 5457-5467, 1991.

Lundin, R., A. Zakharov, R. Pellinen, H. Borg, B. Hultqvist, N. Pissarenko, E. M. Dubinin, S. W. Barabash, I. Liede, and H. Koskinen, Plasma composition measurements of the Martian magnetosphere morphology, *Geophys. Res. Lett., 17*, 877-880, 1990.

Lundin, R., E. M. Dubinin, H. Koskinen, O. Norberg, N. Pissarenko, and S. W. Barabash, On the momentum transfer on the solar wind to the Martian topside ionosphere, *Geophys. Res. Lett., 18*, 1059-1062, 1991.

Mihalov, J. D., J. H. Wolfe, and D. S. Intriligator, Pioneer Venus plasma observations of the solar wind-Venus interaction, *J. Geophys. Res., 85*, 7613-7624, 1980.

Moore, K. R., E. E. Scime, H. O. Funsten, D. J. McComas, and M. F. Thomsen, Low-energy neutral atom emission from the Earth's magnetosphere, *Opt. Eng., 33*, 342-348, 1994.

Nagy, A. F., J. Kim, and T. E. Cravens, Hot hydrogen and oxygen atoms in the upper atmospheres of Venus and Mars, *Ann. Geophys., 8*, 251-256, 1990.

Owen, T., J. P. Maillard, C. de Bergh, B. L. Lutz, Deuterium on Mars: The abundance of HDO and the value of D/H, *Science, 240*, 1767-1770, 1988.

Russell, C. T., T. I. Gombosi, M. Horanyi, T. E. Cravens, and A. F. Nagy, Charge-exchange in the magnetosheaths of Venus and Mars: A comparison, *Geophys. Res. Lett., 10*, 163-164, 1983.

Shinagawa, H., and T. E. Cravens, The ionospheric effects of a weak intrinsic magnetic field at Mars, *J. Geophys. Res., 97*, 1027-1035, 1992.

Spreiter, J. R., A. L. Summers, and A. Y. Alksne, Hydromagnetic flow around the magnetosphere, *Planet. Space Sci., 14*, 223-253, 1966.

Stebbings, R., F., A. C. H. Smith, and H. Erhardt, Charge transfer between oxygen atoms and O^+ and H^+ ions, *J. Geophys. Res., 69*, 2349-2355, 1964.

Tanaka, T., Configurations of the solar wind flow and magnetic field around the planets with no magnetic field: Calculation by a new MHD simulation scheme, *J. Geophys. Res., 98*, 17,251-17,262, 1993.

Vaisberg, O. L., J. G. Luhmann, and C. T. Russell, Plasma observations of the solar wind interaction with Mars, *J. Geophys. Res., 95*, 14,841-14,852, 1990.

Williams, D. J., E. C. Roelof, and D. G. Mitchell, Global magnetospheric imaging, *Rev. Geophys., 30*, 183-208, 1992.

Yeroshenko, Y., W. Riedler, K. Schwingenschuh, J. G. Luhmann, M. Ong, and C. T. Russell, The magnetotail of Mars: Phobos observations, *Geophys. Res. Lett., 17*, 885-888, 1990.

Zhang, M. H. G., J. G. Luhmann, A. F. Nagy, J. R. Spreiter, and S. S. Stahara, Oxygen ionization rates at Mars and Venus: Relative contributions of impact ionization and charge exchange, *J. Geophys. Res., 98*, 3311-3318, 1993a.

Zhang, M. H. G., J. G. Luhmann, S. W. Bougher, and A. F. Nagy, The ancient oxygen exosphere of Mars: Implication for atmosphere evolution, *J. Geophys. Res., 98*, 10,915-10,923, 1993b.

S. Barabash, Swedish Institute of Space Physics, P.O. Box 812, S-98128 Kiruna, Sweden. (e-mail: stas@irf.se)

E. Kallio, Finnish Meteorological Institute, Geophysical Research, P.O. Box 503, FIN-00101, Helsinki, Finland. (e-mail: esa.kallio@fmi.fi)

J. G. Luhmann, Space Sciences Laboratory, University of California, Berkeley, CA 94720. (e-mail: jgluhman@sunspot.ssl.berkeley.edu)

(Received March 20, 1997; revised May 29, 1997;
accepted June 5, 1997.)